Neurobiology of Disease

Early Inflammation Dysregulates Neuronal Circuit Formation *In Vivo* via Upregulation of IL-1β

Cynthia M. Solek,[*] Nasr A.I. Farooqi,[*] Niklas Brake, Philip Kesner, Anne Schohl, Jack P. Antel, and Edward S. Ruthazer

Department of Neurology and Neurosurgery, Montreal Neurological Institute-Hospital, McGill University, Montreal, Quebec H3A 2B4, Canada

Neuroimmune interaction during development is strongly implicated in the pathogenesis of neurodevelopmental disorders, but the mechanisms that cause neuronal circuit dysregulation are not well understood. We performed *in vivo* imaging of the developing retinotectal system in the larval zebrafish to characterize the effects of immune system activation on refinement of an archetypal sensory processing circuit. Acute inflammatory insult induced hyperdynamic remodeling of developing retinal axons in larval fish and increased axon arbor elaboration over days. Using calcium imaging in GCaMP6s transgenic fish, we showed that these morphologic changes were accompanied by a shift toward decreased visual acuity in tectal cells. This finding was supported by poorer performance in a visually guided behavioral task. We further found that the pro-inflammatory cytokine, interleukin-1β (IL-1β), is upregulated by the inflammatory insult, and that downregulation of IL-1β abrogated the effects of inflammation on axonal dynamics and growth. Moreover, baseline branching of the retinal ganglion cell arbors in IL-1β morphant animals was significantly different from that in control larvae, and their performance in a predation assay was impaired, indicating a role for this cytokine in normal neuronal development. This work establishes a simple and powerful non-mammalian model of developmental immune activation and demonstrates a role for IL-1β in mediating the pathologic effects of inflammation on neuronal circuit development.

Key words: autism spectrum disorder; IL-1β; maternal immune activation; retinotectal; visual acuity; zebrafish

---

Significance Statement

Maternal immune activation can increase the risk of neurodevelopmental disorders in offspring; however, the mechanisms involved are not fully understood. Using a non-mammalian vertebrate model of developmental immune activation, we show that even brief activation of inflammatory pathways has immediate and long-term effects on the arborization of axons, and that these morphologic changes have functional and behavioral consequences. Finally, we show that the pro-inflammatory cytokine IL-1β plays an essential role in both the effects of inflammation on circuit formation and normal axonal development. Our data add to a growing body of evidence supporting epidemiological studies linking immune activation to neurodevelopmental disorders, and help shed light on the molecular and cellular processes that contribute to the etiology of these disorders.

Introduction

Prenatal inflammation caused by maternal immune activation (MIA) has been linked to deficits in social interaction, cognition, emotional processing, sensorimotor gating, and executive functions, which are common psychopathological features of several neurodevelopmental disorders (Meyer et al., 2011). Epidemiological studies of large human cohorts have demonstrated a correlation between severe infection during pregnancy and the increased likelihood of neurodevelopmental disorders, such as schizophrenia (Brown and Derkits, 2010) and autism spectrum disorder (ASD) in offspring (Atladóttir et al., 2010). Other lines of evidence, including postmortem brain analyses and preclinical studies in animal models, implicate MIA and continued immune dysregulation in the etiology of neurodevelopmental disorders (Khandaker et al., 2015; Müller et al., 2015; Stuart et al., 2015; Estes and McAllister, 2016; Nakagawa and Chiba, 2016; Mottahedin et al., 2017; Solek et al., 2018). Despite

some contradictory findings, the data point to increased levels of inflammatory cytokines in serum and brain tissue, and abnormal activation of microglial cells both during development and later in life in patients. Moreover, accumulating evidence from clinical studies shows alterations in visual perception and processing in individuals with ASD (Simmons et al., 2009; Robertson et al., 2014; Anketell et al., 2015; Bakroon and Lakshminarayanan, 2016; Robertson and Baron-Cohen, 2017) and schizophrenia (Khosravani and Goodarzi, 2013; Silverstein and Rosen, 2015; King et al., 2017).

Functional brain imaging has identified dysregulated circuit connectivity in individuals with ASD (Heinsfeld et al., 2018; Jack, 2018; Chen et al., 2019). Postmortem examination of ASD brains has also revealed disorganized gray and white matter, decreased volume of neuronal somata, increased neuropil, and increased numbers of neurons (Varghese et al., 2017). Given the paucity of available human postmortem samples and the limited resolution of brain imaging in patients, animal model studies are essential to better characterize the neuronal deficits in these disorders and the processes leading to these defects. Studies in animal models of MIA, mostly in rodents, using administration of polyinosinic:polycytidylic acid or lipopolysaccharide (LPS) to induce immune activation, have demonstrated defects in neurogenesis, cortical organization, neuronal morphology, and synaptic properties (Solek et al., 2018). The externally developing, genetically amenable and transparent zebrafish larva, while not strictly speaking an MIA model, is an excellent alternate vertebrate model to examine the effects of inflammatory insults on the formation and growth of neural circuits during development.

We used *in vivo* time-lapse imaging in a well-described developing circuit, the zebrafish retinotectal projection (see Fig. 1A), to follow the specific effects of acute inflammatory insult on the developing nervous system over time. We devised our inflammatory stimulus protocol to reflect a relatively severe infection paradigm at a time stage corresponding roughly to late second/early third trimester of human development.

Here we show that a brief inflammatory insult induces morphologic activation of microglia and expression of the pro-inflammatory cytokine interleukin-1β (IL-1β) and increases the rate of branching dynamics in developing retinal ganglion cell (RGC) axons. The arbors become larger and more complex several days following the inflammatory stimulus. Moreover, inflammation significantly alters the visual response properties of tectal cells measured with a genetically encoded calcium indicator, and visually guided behavior of the larvae, suggesting functional consequences of the morphologic changes observed. Our experiments additionally revealed a key role for the pro-inflammatory cytokine IL-1β in mediating the effects of LPS-induced inflammation on neurons, as well as in regulating normal RGC axon arborization in the brain.
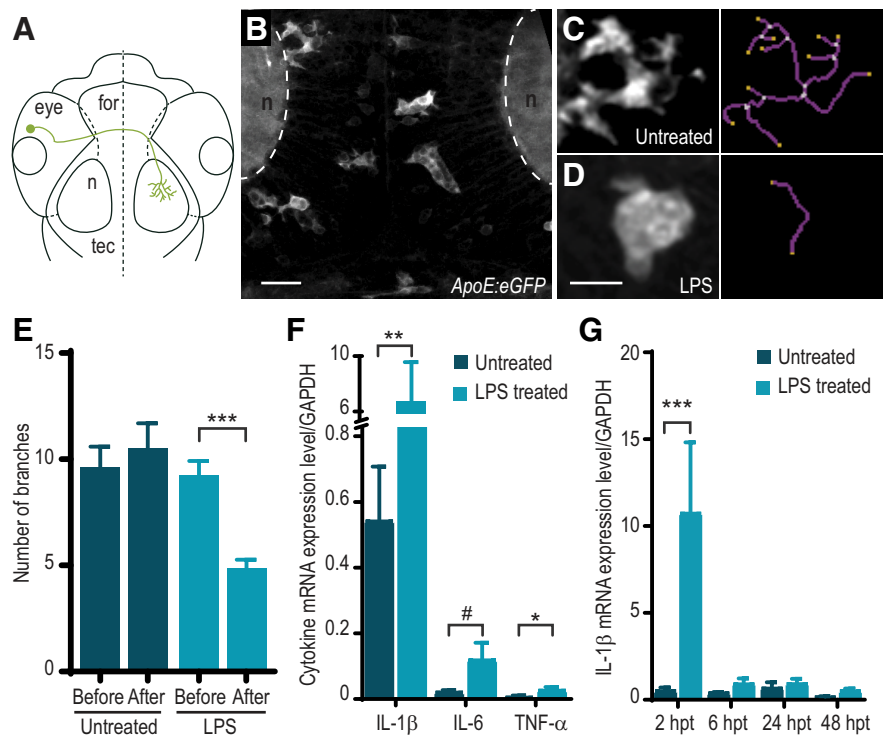

Figure 1. Treatment of zebrafish larvae with LPS causes microglial activation and increased cytokine expression. *A*, Schematic representation of an RGC in the zebrafish larval brain. for, forebrain; n, neuropil; tec, optic tectum. *B*, Microglia have a ramified morphology under normal conditions. Z-projection image of the tectum of a 3 dpf *Tg(ApoE:GFP)* zebrafish. *C–E*, Microglia exhibit morphologic changes in response to LPS. Morphology of microglia following control (*C*) and LPS treatment (*D*). Right, Skeletonized views. *E*, Quantification of number of branching ramifications per microglia in control and LPS-treated *Tg(ApoE:GFP)* larvae at 3 dpf. *n* = 53 cells from 4 animals (control); 91 cells from 7 animals (LPS). ***$p < 0.001$; two-way ANOVA with Sidak correction for multiple comparisons. *F*, Treatment of zebrafish larvae with LPS at 3 dpf causes an increase in mRNA levels of cytokines IL-1β, IL-6, and TNF-α measured by qRT-PCR. mRNA levels were assayed in WT larvae following a 2 h treatment with LPS at 3 dpf or in untreated controls (IL-1β: *n* = 6 untreated, *n* = 7 LPS-treated; IL-6: *n* = 4 untreated, *n* = 4 LPS-treated; TNF-α: *n* = 6 untreated, *n* = 6 LPS-treated). *$p < 0.05$; **$p < 0.01$; #$p = 0.057$; Mann–Whitney test. *G*, IL-1β cytokine mRNA levels measured by qRT-PCR. mRNA levels were assayed in WT larvae at 2 h post-treatment (hpt), 6, 24, and 48 hpt following a 2h treatment with LPS at 3 dpf or in untreated controls (2 hpt: *n* = 7 untreated, *n* = 9 LPS-treated; 6 hpt: *n* = 3 untreated, *n* = 3 LPS-treated; 24 hpt: *n* = 4 untreated, *n* = 4 LPS-treated; 48 hpt: *n* = 3 untreated, *n* = 3 LPS-treated). ***$p < 0.001$; Mann–Whitney test. Error bars indicate SEM. Scale bars, 10 μm.

Materials and Methods

Animal care. All animal use protocols were reviewed and approved by the Animal Care Committee of the MNI, McGill University. Zebrafish maintenance and breeding were performed according to standard techniques (Westerfield, 2000). Embryos were raised in E3 embryo medium at 28.5°C; 0.2 mM phenylthiourea was added to embryo water after 24 h of development to inhibit pigment formation for *in vivo* imaging experiments. Embryos for imaging of microglia were obtained by natural spawning from the *Tg(ApoE:GFP)* transgenic line (Peri and Nüsslein-Volhard, 2008) generously provided by Francesca Peri (EMBL). Embryos for calcium imaging were obtained from the *Tg(elav3:H2B-GCaMP6s)* transgenic line (Vladimirov et al., 2014), crossed with compound *roy;nacre* double homozygous mutants (*casper*, which lack melanocyte and iridophore pigmentation) generously provided by Misha B. Ahrens (Janelia Campus, Howard Hughes Medical Institute). All other experiments were performed using WT embryos from Tüpfel long fin zebrafish (kind gift of Pierre Drapeau, University of Montreal).

Treatment. LPS from *Salmonella enterica serovar typhimurium* (Sigma Millipore, L6511) was added to zebrafish E3 embryo medium at a final concentration of 25–30 μg/ml. After 2 h, larvae were removed from LPS and rinsed thoroughly in E3 embryo medium. Notably, we were unable to elicit inflammatory responses with LPS from *Escherichia coli*. Injection of 2-4 pl LPS (750 μg/ml) with phenol red (final concentration 0.125%) into the pericardium of the 3 dpf larvae was performed as described, 2 h before sample collection (Christou-Savina et al., 2015).

Microglia number and morphology analysis. Tg(ApoE:GFP) larvae were treated with LPS for 2 h or mock-treated as controls at 3 dpf. For microglia morphology analysis, images of the tectum were acquired immediately after treatment, on an upright confocal microscope custom-converted for two-photon imaging, using a $60\times$ water immersion objective (NA 1.1) with excitation light provided by a Ti:sapphire femtosecond pulsed laser (Maitai BB, Spectra-Physics). The 1 μm interval *z*-series stacks were acquired with Fluoview 5.0 software (Olympus). The number of branches for each microglia was measured in Fiji using the Analyze Skeleton function on the despeckled and thresholded image (Morrison and Filosa, 2013). For microglia number analysis, images of the tectum were acquired as described above immediately after treatment and again in the same larvae at 4, 5, and 6 dpf. Microglia were manually counted using the 3D viewer plugin in Fiji, with the experimenter blinded to treatment condition.

qRT-PCR. Twenty to 35 zebrafish larvae of the appropriate stage were collected in a microcentrifuge tube and killed by snap-freezing in an ethanol-dry ice bath. RNA was extracted with TRI Reagent (Invitrogen) and purified with RNEasy mini-kit (QIAGEN) according to a standard protocol (Marín and Rubenstein, 2001), including a 30 min DNase (QIAGEN) digest. Reverse-transcription was performed on 1 μg of total RNA with Superscript II or Superscript IV (Invitrogen) according to the manufacturer's instructions. TaqMan qRT-PCR (Invitrogen) was performed using the following assays: GAPDH (Dr03436842_m1), IL-1β (Dr03114368_m1), and TNF-α (Dr03126850_m1). Custom probes were designed against *Danio rerio* IL-6 (forward: 5′-TCAGAC CGCTGCCTGTCTA-3′; reverse: 5′-CACGTCAGGACGCTGTAGAT-3′). No amplification was seen in no-RT and no-template controls. Data were normalized to the housekeeping gene GAPDH, and relative gene expression was calculated according to the ΔC_t method (Livak and Schmittgen, 2001).

RGC axon labeling and morpholino injection. Linearized and purified plasmid DNA at a total concentration of 40 ng/μl was injected into the cytoplasm of 1 or 2 cell stage fertilized zebrafish eggs. The following plasmids were used and have been previously described: *pBrn3c:Gal4* (Xiao et al., 2005) (gift of Herwig Baier, MPI Martinsried); and *pUAS: mYFP* (Schroeter et al., 2006) (gift of Leanne Godinho, TUM). Larvae were screened for expression at 3 dpf. The IL-1β morpholino (5′-TAACCAGCTCTGAAATGATGGCATG-3′), which has been previously described (Banerjee and Leptin, 2014), and a standard control morpholino were obtained from Gene Tools and were pressure-injected into the yolk of 1 or 2 cell stage fertilized embryos at a concentration of 0.25 mM. To test the efficacy of the morpholino, pCS-IL1β-ATGmo-eGFP was generated by inserting a 146 bp fragment of *IL-1β* encompassing the region of morpholino binding into the pCS-eGFP plasmid, in-frame with eGFP. The plasmid was linearized using NotI, and capped mRNA was transcribed using an SP6 RNA polymerase *in vitro* transcription kit (mMESSAGE mMACHINE SP6; Invitrogen); 2 nl of solution was injected at an RNA concentration of 2 ng/μl, with Control or IL-1β morpholino oligonucleotide (MO) in 1 cell stage embryos, and the presence of green fluorescence was assessed at 24 hpf. Images were taken using a Carl Zeiss Imager.M1 fluorescent microscope equipped with an Axiocam 503 camera and uniformly adjusted for contrast and brightness using Adobe Photoshop.

Two-photon in vivo imaging. Unanesthetized zebrafish larvae at 3-6 dpf were mounted in 1.2%-1.4% low-melting point agarose in custom-built imaging chambers. Imaging was performed on a custom-built upright two-photon microscope, as described above, using excitation light at 910 nm. The 1 μm interval *z*-series stacks were acquired with Fluoview 5.0 software (Olympus). For daily imaging, larvae were gently removed from the agarose and returned to regular housing between imaging sessions.

Image processing. Three- or four-dimensional image stacks were denoised using CANDLE software (Coupé et al., 2012). Skin autofluorescence was manually removed in ImageJ software (National Institutes of Health). As zebrafish RGC axons are highly planar, *XYZ* stacks were *Z*-projected for further analysis. Dynamo software (Kurt Haas) was used to reconstruct axonal arbors and quantify total arbor length, total number of branches, rates of branch addition, loss, and number of transient branches.

Measurement of larval size. Larvae were acquired through natural fertilization from three separate matings on 3 separate days. At 6 dpf, larvae from LPS-treated and untreated groups were placed on custom slides under a dissecting microscope fitted with a 3D-printed cell phone holder. Images acquired with an Android smartphone were analyzed with the Micro-measurements application (Octavian Fometescu) calibrated with a micro-ruler.

Calcium imaging and analysis. Tg(elav3:H2B-GCaMP6s) were treated with LPS for 2 h at 3 dpf. At 6 dpf, larvae were imbedded in 1.4% low-melting point agarose in custom-built imaging chambers, with the right eye facing a side window constructed from a glass coverslip. Visual stimuli were generated by a custom MATLAB code and displayed on a 108×64 mm HDMI display with 800×480 resolution. A red Wratten filter #29 or red optical cast plastic filter (565LP) was positioned in front of the display to filter out light at the wavelengths detected for GCaMP signal. Brightness stimuli consisted of 0.2 s full-field flashes, presented at 10 luminance levels. Spatial frequency stimuli consisted of sinusoidal gratings at 0.0073, 0.0147, 0.0293, 0.0367, 0.0587, 0.0733, 0.1173, 0.1466, 0.1833, 0.2346, 0.2933, 0.3666, 0.5865, 0.7332, 1.173, and 1.4663 cycles per degree of visual angle (cyc/deg) counterphasing at 5 Hz for 1 s. Each stimulus, including null stimuli, which were used to estimate baseline signal variance in the absence of a response, was presented 10 times in random order with 7 s rest periods in between presentations. Reproducible positioning distance between the larva and the display was achieved by a custom 3D-printed chamber holder. Pulsed infrared excitation light was generated by either a Mai Tai Ti: Sapphire or InSight X3 laser (Spectra-Physics) tuned to 910 nm. Emitted light was collected with a 20×1.0 NA water immersion objective (Olympus) and detected using a gallium arsenide phosphide (GaAsP) photomultiplier (ThorLabs). Images (512×512 pixels) of the left optic tectum were acquired at a frame rate of 30 Hz by galvo-resonant scanning. XYZT series were collected in 10 μm steps using a piezoelectric focusing collar (PI). This allowed for volumetric data consisting of four focal planes (with 2 flyback frames) to be collected at a rate of $\sim$5 Hz. Scanning and image acquisition were controlled by ThorImage, with ThorSync (ThorLabs) for synchronization of stimulus presentation to a 5 V trigger to a National Instruments analog-to-digital converter. Images were registered for drift in *x-y* when needed. Any imaging experiment which showed significant *z*-drift was discarded. GCaMP6s targeted to cell nuclei was used to segment ROIs for analysis by ImageJ processing and particle analysis functions called from MATLAB. Fluorescence intensity change within each ROI was calculated and normalized to baseline ($\Delta F/F_0$); the baseline signal was defined at each stimulus presentation as the average fluorescence intensity in a 1200 ms temporal window centered on the stimulus onset. For all timepoints between stimulus presentations, baseline was calculated as the linear interpolation between the previous and subsequent presentation baseline values. An ROI's response to each stimulus was calculated as the average $\Delta F/F_0$ signal during a 5 s window starting after presentation of the stimulus. For each ROI, a *t*-statistic for each stimulus was computed relative to the null distribution generated by the responses to blank stimuli, using the following formula:

$$t = \frac{\overline{X_i} - \overline{X_0}}{\sqrt{\frac{s_i^2}{N_i} + \frac{s_0^2}{N_0}}}$$

where $\overline{X_i}$ is the average reponse to stimulus i, $\overline{X_0}$ is the average response to the null stimulus, s_i and s_0 are the respective sample variances, and N_i and N_0 are the respective sample sizes. ROIs with a *t*-statistic >2.5 for at least 1 stimulus were retained for further analysis. For brightness stimuli, a linear model between response strength and stimulus strength was estimated using the ordinary least-squares method. All ROIs with $R^2 > 0.531$ were used from each larva and pooled for group-level analysis. This R^2 cutoff value was selected based on the mean 75th quartile of the linear regression R^2 for all the fish in both datasets. For spatial frequency stimuli, a principal components analysis was run on the pooled

responses of all ROIs to each spatial frequency. The first principal component accounted for >50% of the variance in the responses to spatial frequencies and reflected a sigmoidal-shaped response profile. Accordingly, we fit the responses of every ROI to the sigmoidal function as follows:

$$\Delta F/F_0(f) = a_1 + \frac{a_2}{1 + \exp\left(\frac{f - SF_{50}}{k}\right)}$$

where $\Delta F/F_0$ is the response of the ROI as a function of spatial frequency, a_1 and a_2 are scaling factors, SF_{50} is the spatial frequency that elicited a half-maximal response, and k is the slope factor. The goodness-of-fit (R^2) was measured for each ROI, and all ROIs with $R^2 > 0.85$ were kept for further analysis. This threshold was chosen arbitrarily; the results of our analysis were robust to an increased or decreased threshold. We further excluded cells whose estimated SF_{50} fell outside the range of spatial frequencies that were presented as stimuli, as well as cells with slope factors that were too steep ($k < 0.0075$). This slope factor threshold was chosen to exclude cells displaying binary rather than graded responses, but ultimately the inclusion or exclusion of these cells did not change the outcome of our analysis. All MATLAB code used can be found on GitHub (https://github.com/niklasbrake/LPS-2020).

Predation assay. *Paramecium multimicronucleatum* were obtained from Carolina Biological Supplies. The 6 dpf zebrafish larvae (untreated and LPS-treated at 3 dpf) were assessed for overall health with a 30 min free-swim assay using DanioVision (Noldus). Any fish that swam less than half the average distance traveled by all fish in the same treatment group was discarded. One to three larvae were transferred to a 35 mm Petri dish along with 25-75 paramecia. The dish was placed on a polarizing glass plate, illuminated obliquely, and imaged with a Logitech C922x Pro Stream 1080P Webcam for 20-40 min. All recorded prey capture events were analyzed using ImageJ software (National Institutes of Health). Predation capability was assessed differently in control MO, IL-1β MO, untreated, and LPS-treated larvae. Following free-swim evaluation as described above, 3 larvae were added to a 35 mm Petri dish along with 25-75 paramecia. A 3-5 s video was acquired for each plate at 30 fps, before the addition of the zebrafish larvae, and hourly thereafter for 5 h. The movies were analyzed *post hoc*, by taking the *t*-projection of each frame with the first frame subtracted, allowing paramecium motion to be readily visible as trails. Paramecia were counted at each time point, with the experimenter performing the analysis blind to the condition and the timing of movie acquisition. The original movies were consulted to resolve any ambiguities in the *t*-projections. Each condition was performed in duplicate on 5 separate days ($n = 10$ for each treatment group). The paramecium prey decline constant was obtained using MATLAB by fitting the data to an exponential function derived from the Lotka-Volterra differential equations, keeping predator number constant. It was previously reported that this constant does not depend on the number of paramecia at the start of the experiment (Smear et al., 2007).

RNAscope/immunohistochemistry. *Tg(ApoE:GFP)* zebrafish larvae (3 dpf, untreated and LPS-treated) were fixed in 4% PFA/PBS overnight at 4°C and washed 3 times in cold 1× PBS and then equilibrated with 30% sucrose in PBS overnight at 4°C. The samples were then incubated in 1:2 30% sucrose:OCT Compound (Tissue-Tek) for 30 min and frozen in cryomolds; 14 μm cryosections were obtained with a CM1850 cryostat (Leica Microsystems). RNAscope was performed following the manufacturer's directions (ACD Bio), using a *Dr-IL-1β* probe set (catalog #432971). Sections were then washed in PBST (PBS with 0.1% Tween 20) and blocked in 10% calf serum in PBST for 2 h at room temperature. Slides were incubated with chicken anti-GFP (Abcam, ab13970) primary antibody in 1% calf serum in PBST overnight at 4°C. Sections were then washed 3 times for 15 min with PBST and incubated with goat anti-chicken Alexa-488-conjugated secondary antibody (Invitrogen, A-11039) in 1% calf serum in PBST for 2 h at room temperature. Sections were washed 3 times for 15 min with PBST, and nuclei were visualized with DAPI before mounting in ProLong Gold (Invitrogen, P10144). Images were acquired on a Carl Zeiss LSM880 confocal microscope, pseudocolored, and uniformly adjusted for contrast and brightness using Adobe Photoshop.

Statistical analysis. All statistical analyses were performed using GraphPad Prism 8.4.1 software. For qRT-PCR, Mann–Whitney tests were performed to compare expression in untreated samples with those treated with LPS. For dynamics imaging analysis, total number of branches added, lost, or transient branches were normalized to the average number of total branches for each RGC during the imaging period. The rate of branch addition, loss was then calculated by dividing by the number of time points. The rate pretreatment was set to 1, and increase or decrease in the rate following treatment was calculated as the ratio of the rate post-treatment to pretreatment. Two-way repeated-measures ANOVA comparisons of control MO and no MO samples for all conditions showed no significant difference between the groups; these were pooled to increase the statistical power of subsequent analyses. Two-way repeated-measures ANOVA was performed for each set of data to assess statistical significance of the effect of LPS treatment. For daily imaging analysis, total arbor length and total branch numbers were compared using two-way repeated-measures ANOVA. Comparison of the control MO and no MO animals showed that control MO injection caused no significant differences in growth; these two groups were pooled for analysis. Outliers were identified using the ROUT method (Q = 1%). Two-way repeated-measures ANOVA was performed for each set of data to assess statistical significance of the effect of LPS treatment. For the branch size distribution analysis, we performed Wilcoxon tests of the frequency distribution of all the branch lengths in each group for each time point separately. For GCaMP6s imaging analysis of response to brightness stimuli, unpaired two-tailed *t* tests were performed on the number of ROIs/fish that met linear regression criteria (see above). No significant difference in the number of ROIs meeting criterion was found between treatment groups. Mann–Whitney tests were performed on the pooled values of slope and *x*-intercept as these measures failed Kolmogorov–Smirnov tests for normality. For the response to spatial frequency stimuli, Wilcoxon rank sum test was used to compare distributions of SF_{50} values. For the predation experiments, Welch's *t* test was performed to compare the predation event parameters; Kruskal–Wallis tests were performed to compare prey decline constants. For RNAscope analysis, Kruskal–Wallis tests were performed to verify the significant difference in % skin expressing IL-1β and number of IL-1β puncta per microglia.

Results

LPS causes an inflammatory response in zebrafish larvae

LPS is a bacterial endotoxin which has been shown to rapidly and robustly trigger an inflammatory response in a variety of animals, including zebrafish (Xie et al., 2021). We therefore stimulated an inflammatory reaction in 3 dpf zebrafish larvae by immersion for 2 h in E3 rearing medium containing LPS. We opted for waterborne delivery of LPS rather than injection since it more closely resembles the fetal exposure to a mother's response to infection during pregnancy. Indeed, although some pathogens manage to colonize the placenta, very few ever reach the fetal circulation (Robbins and Bakardjiev, 2012). To ascertain whether this brief exposure by immersion was sufficient to induce an inflammatory reaction in the CNS of zebrafish larvae, we used *Tg(ApoE:GFP)* to image microglia in the optic tectum by *in vivo* two-photon microscopy (Fig. 1A,B). Microglia in the zebrafish have a spectrum of morphologies and activation states from ramified-surveillant to amoeboid-activated (Peri and Nüsslein-Volhard, 2008; Svahn et al., 2013). We quantified the number of processes extended by each microglial cell as a metric of morphologic complexity (Fig. 1C,D). Two hours of LPS exposure induced microglia to adopt more amoeboid morphologies, reflected in a lower number of branches, consistent with immune activation (Fig. 1E). Pro-inflammatory cytokines, such as TNF-α, IL-6, and IL-1β, have been shown to be robustly upregulated
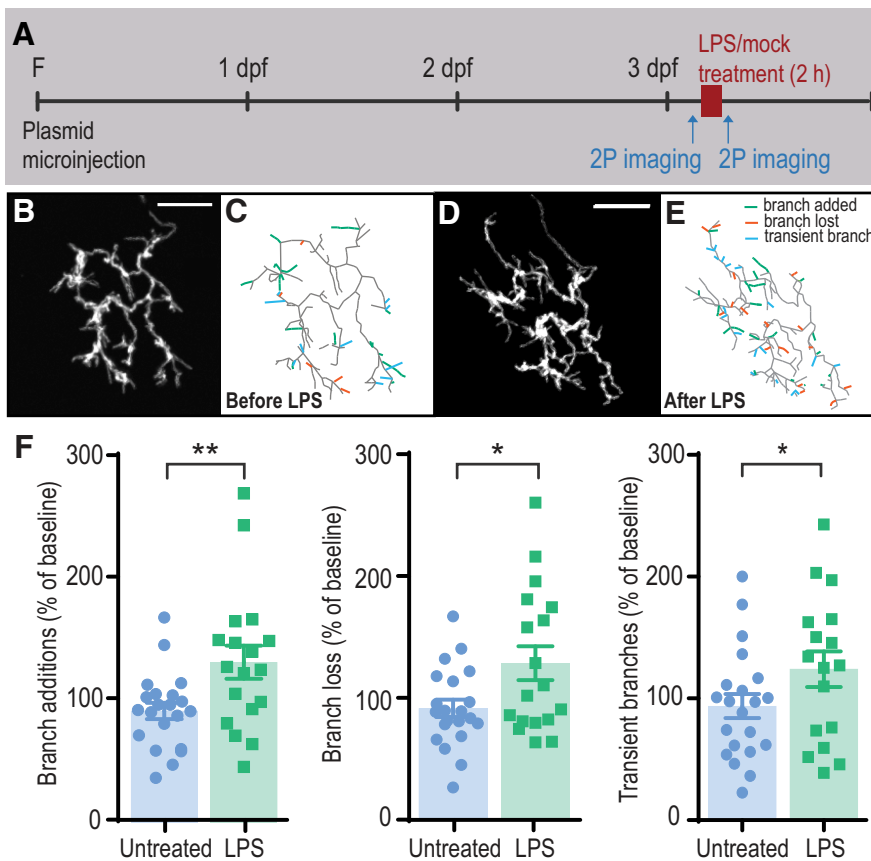
Figure 2. Treatment of zebrafish larvae with LPS causes increased RGC branching dynamics. *A*, Experimental design: single RGCs expressing mYFP were imaged at 3dpf before and after 2 h treatment with LPS or mock treatment control. *B–E*, Arbors are shown as projected *z* stacks (*B,D*) and as reconstructed skeletons (*C,E*). Green represents branch additions during a 36 min imaging period. Red represents losses. Blue represents transient branches. *F*, Rates of branch addition, branch loss, and transient branches are significantly increased following LPS exposure (*n* = 21 untreated; *n* = 18 LPS-treated). **$p < 0.01$; *$p < 0.05$; two-way repeated-measures ANOVA. Error bars indicate SEM. Scale bars, 25 μm. F, Fertilization.
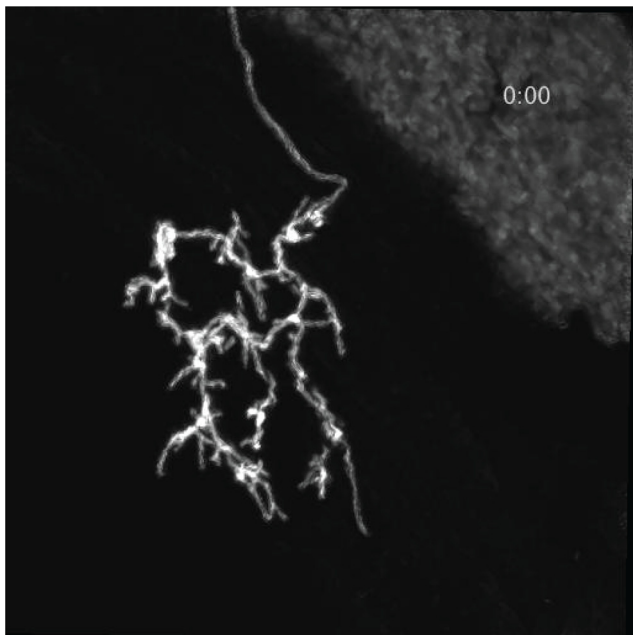
Movie 1. Time-lapse *in vivo* two photon microscopy of individual RGC axons in 3 dpf zebrafish. Z-stack images were taken every 6 min for 36 min before and after 2 h exposure to LPS. Maximum intensity projections of denoised images are shown (see Materials and Methods). [View online]

in zebrafish in response to LPS (Novoa et al., 2009; Yang et al., 2014; Hasegawa et al., 2017). We performed qRT-PCR on zebrafish larvae after 2 h of exposure to LPS at 3 dpf. Our results indicate a rapid induction of IL-1β (12.3-fold), IL-6 (5.3-fold), and TNF-α (4.1-fold) mRNA expression (Fig. 1F). We found that mRNA levels for inflammatory cytokines, such as IL-1β, return to baseline within 6 h of LPS treatment (Fig. 1G).

LPS-induced inflammation causes immediate changes in RGC axon growth

To determine the effects of LPS on the arborization of developing axons, we expressed monomeric yellow fluorescent protein (mYFP) in RGCs by injecting one-cell stage embryos with *Brn3c: Gal4* and *UAS:mYFP*, and selected mosaic embryos with sparse labeling of RGC axons (Xiao et al., 2005). At 3 dpf, we performed time-lapse two-photon imaging of individual RGC axon arbors in the optic tectum (every 6 min for 36 min; Fig. 2A–E; Movie 1) during an initial baseline period and immediately after 2 h of exposure of the larva to LPS, and then digitally reconstructed the arbors to obtain 4-dimensional morphometric data. We performed the same analysis for cells in control animals. Comparison of the two imaging periods demonstrates that LPS treatment increases rates of axonal branch addition and loss (Fig. 2F). The number of transient branches (those that were formed and then lost during the imaging period) is similarly increased by LPS treatment (Fig. 2F), consistent with an overall increase in branching dynamics. These data reveal that a short exposure to an inflammatory stimulus is sufficient to cause alterations in axonal branch dynamics.

LPS-induced inflammation causes lasting changes in RGC axon growth

Epidemiological studies suggest that short periods of inflammation during intrauterine development can contribute to lifelong alterations in neuronal function which may manifest as ASD or schizophrenia (Meyer et al., 2011). To establish whether a short inflammatory insult results in persistent effects on neuronal morphology, we imaged axons daily from 3 to 6 dpf, following a 2 h exposure to LPS at 3 dpf (Fig. 3A). This corresponds to a period starting 1 d after the RGC axons enter the optic tectum and begin to arborize (Poulain et al., 2010) until growth and elaboration of the arbors have essentially reached a plateau. We found that RGCs had larger and more elaborate arbors at 6 dpf in LPS-treated animals compared with control untreated animals (Fig. 3B–E). This difference is not caused by a change in overall growth of the animals since the size of the larvae did not differ significantly between groups at 6 dpf (untreated: 3.92 ± 0.20 mm, *n* = 41; LPS-treated: 3.96 ± 0.19 mm, *n* = 38). This implies that the short period of inflammation triggered by early LPS
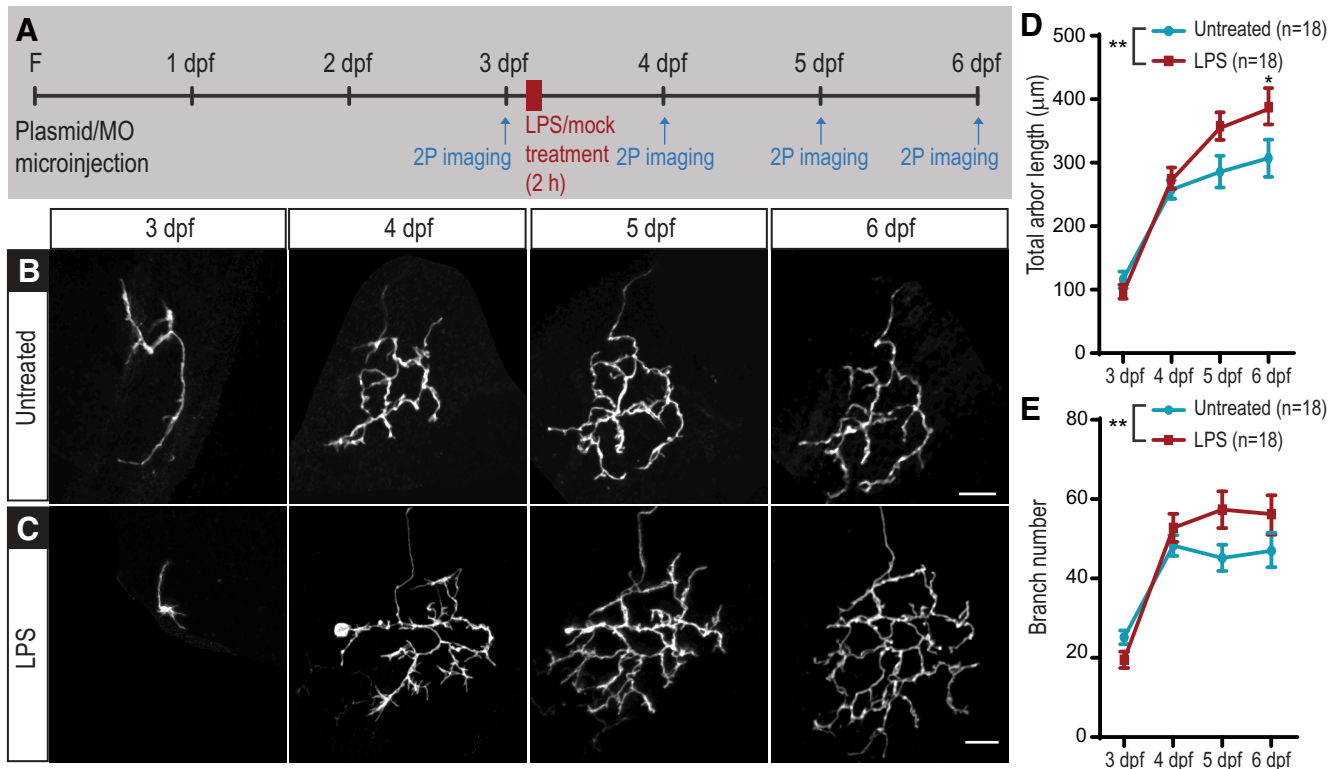
Figure 3. LPS treatment of 3 dpf larvae has long-term effects on RGC arbor growth. ***A***, Experimental design: single RGCs expressing mYFP were imaged at 3 dpf before 2 h of mock (untreated, ***B***) or LPS (***C***) treatment. The same animal was imaged again on the 3 subsequent days. LPS-treated RGCs have larger arbors (***D***) and significantly more branch tips (***E***; $n = 18$ untreated, $n = 18$ LPS). ******$p < 0.01$; two-way repeated-measures ANOVA with Sidak correction for multiple comparisons. Error bars indicate SEM. Scale bar, 25 μm. F, Fertilization.

treatment (Fig. 1*G*) causes sustained changes that affect subsequent neuronal growth and circuit formation over days or longer.

Functional consequences of neuronal development defects caused by inflammation
To determine whether the functionality of the retinotectal circuit is affected by the morphologic changes following LPS treatment, we used calcium imaging to assess the responses of tectal cells to visual stimuli (Fig. 4*A,B*). We performed fast resonant-scanning two-photon *in vivo* imaging in *Tg(elav3:H2B-GCaMP6s)* transgenic zebrafish, which express the genetically encoded calcium indicator GCaMP6s in the nuclei of most neurons, facilitating automated single-cell segmentation of ROIs for analysis (Fig. 4*C*) (Vladimirov et al., 2014). We compared larvae treated at 3 dpf with LPS for 2 h with control animals by measuring the responses of tectal neurons to a set of visual test stimuli at 6 dpf (Fig. 4*A*), corresponding to the last day of imaging in our morphologic study (Fig. 3).

We began by interrogating the sensitivity of tectal cells to brightness level by presenting full-field flashes of varying brightness and analyzing the response properties of individual cells (see Materials and Methods). Many tectal cells displayed a linear relationship between GCaMP6s response and stimulus brightness. To select these cells for analysis, we performed linear regression of response strength ($\Delta F/F_0$) to brightness level for each cell and selected those with an $R^2 > 0.531$ (see Materials and Methods). The number of cells in each fish that met these selection criteria did not significantly differ between the untreated and LPS-treated groups (untreated: 108 ± 12.9 cells, $n = 10$; LPS-treated: 98 ± 17.0 cells, $n = 9$; $t = 0.14$, $p = 0.89$, Student's t test). The x intercept of the regression line for response versus brightness in these cells corresponds to the

brightness sensitivity threshold for flash detection. Brightness sensitivity thresholds did not differ between cells from LPS-treated and control fish, suggesting that, on average, cells respond to the same minimum brightness stimulus in both groups (Fig. 4*D,E*; untreated: 0.085 ± 0.29, $n = 1197$ cells; LPS-treated: 0.097 ± 0.27, $n = 1126$; $p = 0.28$, Mann–Whitney test). On the other hand, the slope of the linear regression line was significantly lower in cells from LPS-treated larvae (Fig. 4*D,F*; untreated: 0.216 ± 0.19, $n = 1197$ cells; LPS-treated: 0.184 ± 0.16, $n = 1126$; $p < 0.0001$, Mann–Whitney test). This indicates that, although the threshold for detection of a flash is similar between groups, the ability to discriminate between brightness levels may be reduced in LPS-treated larvae.

We next evaluated visual response acuity using the same experimental set up as for brightness but presenting counterphasing sinusoidal gratings at a range of spatial frequencies. We fitted the spatial frequency responses of each ROI to a sigmoidal curve, as demonstrated for an example cell in Figure 4*G* and calculated goodness-of-fit, selecting cells with $R^2 > 0.85$. The number of cells in each fish that met this selection criterion did not significantly differ between the untreated and LPS-treated groups (untreated: 50 ± 6.4 cells, $n = 16$; LPS-treated: 40 ± 5.1 cells, $n = 19$; $t = 1.23$, $p = 0.23$, Student's t test). For each selected ROI, we extracted an SF_{50} value, the spatial frequency at which the cell displayed a response equal to half its maximal response strength (Fig. 4*G*, dashed line). A significant shift in the median of the distribution of SF_{50} was observed for LPS-treated animals (untreated: median $= 0.0218$, $n = 798$; LPS-treated: median $= 0.0189$, $n = 760$; $p = 0.00125$, Wilcoxon rank sum test). The median SF_{50} in tectal cells from LPS-treated larvae is shifted toward a lower spatial frequency than that in untreated control cells (Fig. 4*H*). These data suggest that LPS-treated larvae may have slightly lower visual acuity at the level of individual tectal neurons.
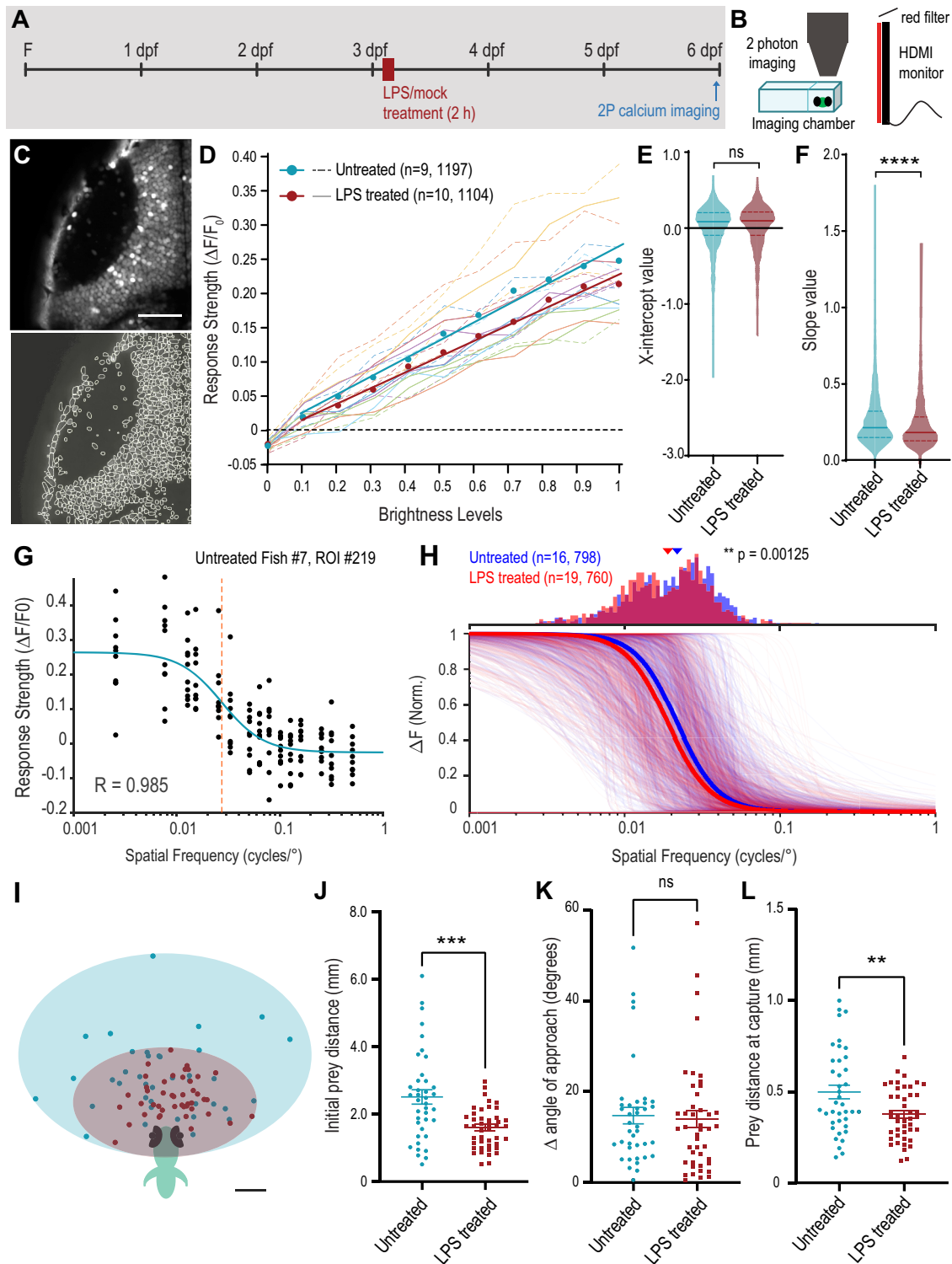
Figure 4. Functional consequences of inflammation on retinotectal circuit function. *A*, Experimental design: *Tg(elav3:H2B-GCaMP6s)* larvae were treated for 2 h with LPS or mock treatment control and imaged at 6 dpf. *B*, Experiment setup: larvae were embedded in low-melting point agarose in a custom chamber and placed in front of a monitor showing visual stimulation protocols. Calcium-induced changes in GCaMP6s fluorescence were recorded with a two-photon microscope. *C*, Example time-projected image from 1 z-plane of the left tectum of a *Tg(elav3:H2B-GCaMP6s)* larva with ROIs auto-identified for data extraction (bottom). *D*, Average response strength ($\Delta F/F_0$) of the significantly responding cells to full-field flash visual stimuli of increasing brightness levels for each larva. Average response strength ($\Delta F/F_0$) of the ROIs for individual fish are indicated by dashed lines (untreated) and full lines (LPS-treated). Circles with corresponding trendlines represent the average of all the ROIs. *E,F*, Comparison of linear regression values for x intercept (*E*) and slope (*F*; untreated $n = 9$ fish, 1197 total ROIs; LPS-treated $n = 10$ fish, 1104 total ROIs). ****$p < 0.0001$. *G*, Response strength of an example cell to each of 10 presentations of visual stimuli consisting of counterphasing sinusoidal gratings of varying spatial frequency. The data are fitted to a sigmoidal curve, and the spatial frequency value at which the cell generates a response of half-maximum strength (SF_{50}) is extracted. *H*, Normalized sigmoidal response curves for all selected cells in untreated (blue, $n = 16$ fish, 798 total ROIs) and LPS-treated (red, $n = 19$ fish, 760 total ROIs) larvae, with average group response curves illustrated with thick lines of corresponding color. The distribution of the SF_{50} values for selected cells is shown in the histogram above. Arrowheads above the histogram represent a shift in the median value of the distribution. **$p = 0.00125$; Wilcoxon rank sum test. *I*, Representation of the position of paramecia at initiation of pursuit by untreated (green, $n = 43$ events, 6 larvae) and LPS-treated larvae (red, $n = 47$ events, 7 larvae). *J–L*, Comparisons of initial prey distance (*J*), difference between the prey angle and the angle of the initial turn (*K*), and the distance of the prey before the final swim bout at the time of capture (*L*). ***$p < 0.001$; **$p < 0.01$; Welch's *t* test. Error bars indicate SEM. Scale bars: *C*, 50 μm; *I*, 0.5 mm. F, Fertilization.

Overall, the above results suggest that LPS treatment alters the wiring of the retinotectal circuit, leading to changes in the functional properties of tectal cells. To assess whether these changes have behavioral consequences, we performed a predation assay (Orger et al., 2004). By 6 dpf, zebrafish larvae no longer derive sufficient nutritional support from yolk, and instead have begun to use vision to scavenge food from the environment. We placed 6 dpf larvae in a Petri dish with paramecia, prey for zebrafish larvae, and recorded capture events (Fig. 4I–L). We measured a number of parameters from each event, including prey distance and angle at initiation of pursuit, initial larva turn, number of swim bouts to successful capture, final turn angle, and distance of prey immediately before capture (Patterson et al., 2013). We found that the average distance of the paramecia at the onset of pursuit was greater in untreated larvae than in LPS-treated animals (Fig. 4I,J). This suggests that LPS-treated larvae may have more difficulty seeing prey at a distance, indicative of poorer visual acuity, in line with our results from GCaMP imaging. Zebrafish larvae typically underestimate the initial turn angle necessary to perfectly align their body axis with the prey to begin pursuit (Patterson et al., 2013). We calculated the difference between the angle of prey location and that of the initial turn (Δ angle of approach) and found no difference between untreated and LPS-treated groups (Fig. 4K). We also found no difference in the number of swim bouts that larvae make between initiation of pursuit and capture (not shown). This suggests that, once LPS-treated larvae see their prey, they are just as efficient in their pursuit. However, the distance of the paramecia at initiation of the final swim bout leading to capture was on average slightly greater in untreated than LPS-treated larvae (Fig. 4L). This provides further evidence to suggest that these animals process visual information differently from controls. In summary, an acute inflammatory insult early in visual system development leads to significant changes in the functional properties of the retinotectal circuit and to visually-guided behavior, with reduced brightness discrimination and visual acuity, manifesting in deficits in prey perception at 6 dpf.

The role of IL-1β in mediating inflammation-induced neuronal defects

We next sought to investigate the molecular mechanisms by which inflammatory insults cause neuronal growth changes. Cytokines, including IL-1β, have physiological functions that include regulation of neurogenesis, neuronal survival, strength of synaptic transmission, and synaptic plasticity (Schneider et al., 1998; Ikegaya et al., 2003; Vezzani and Viviani, 2015). Moreover, IL-1β has been demonstrated to play a role in axonal structural plasticity in mouse slice cultures (Boato et al., 2011, 2013). In our experiments, IL-1β mRNA levels showed robust activation following LPS treatment (Fig. 1F).

To identify the cells that exhibit upregulation in expression of IL-1β in our inflammation model, we performed RNAscope on 3 dpf Tg(ApoE:GFP) larvae, coupled with immunohistochemistry for GFP to label microglia, immediately after 2 h of LPS treatment (Fig. 5). As a positive control for induced IL-1β expression in myeloid cells, including microglia, we performed microinjection of LPS into the pericardium of 3 dpf larvae (Hasegawa et al., 2017)(Fig. 5D,H,L,P). Compared with untreated control samples, animals treated with bath application of LPS showed marked IL-1β mRNA expression in patches of the skin in the fins (Fig. 5B,C, arrowheads), head (Fig. 5F,G, arrowheads), and tail (Fig. 5N,O, arrowheads). Quantification of the acquired images from three separate larvae confirm a significant increase in IL-1β

mRNA in the skin of LPS-treated larvae compared with untreated controls (Fig. 5Q). Expression of IL-1β was also detected in microglia in the tectum (Fig. 5F,G, arrows), the retina (Fig. 5J,K, arrows), and spinal cord (Fig. 5N,O, arrows) of both untreated and LPS-treated animals. The number of IL-1β puncta per microglia was significantly increased in LPS-injected animals (Fig. 5R), consistent with previously published data (Hasegawa et al., 2017).

We hypothesized that reducing IL-1β production with a MO might prevent the immediate effects of LPS. Indeed, we found that the enhancement in RGC axon dynamics in response to LPS exposure was absent in morphant fish injected at the one-cell stage with IL-1β antisense MO (Fig. 6A). Control MO-injected larvae treated with LPS showed an increase in branch additions and loss comparable with that observed in animals without MO (not shown).

We next asked whether increased IL-1β expression was necessary for the long-term arborization changes in RGCs induced by LPS treatment. We performed daily imaging of RGC axons in IL-1β MO-injected animals from 3 to 6 dpf (Fig. 6B–E). We found that IL-1β knockdown prevented the effects of LPS on axonal growth, reflected by similar total arbor length and branch number in LPS and untreated animals (Fig. 6B,C). We verified the efficacy of the morpholino with an IL-1β 5′-UTR-eGFP fusion construct and demonstrated its translation blocking effect in vivo (Fig. 6F,G).

We noticed that basal RGC arbor growth and morphology were different between IL-1β morphants and control MO animals. RGC axonal arbors in control MO larvae plateau in both size and branch number by 5 dpf, whereas those in IL-1β MO larvae continue to grow and add branches, having significantly more branches than control cells by 6 dpf (Fig. 7A). In LPS-treated animals, the RGC growth curves are also different, with the IL-1β MO-injected cells eventually reaching a total length comparable with those in control MO samples, but with significantly more total branches than controls at 6 dpf (Fig. 7B). Finally, RGC axons in LPS-treated, IL-1β MO-injected larvae have more fine filopodia (<2 μm) than LPS-treated control MO-injected animals, which resulted in a significant difference in the branch size distributions between IL-1β MO-injected and control MO-injected larvae at 6 dpf (Fig. 7C,D; $p < 0.05$, Wilcoxon test). No such difference was seen comparing control MO and no MO cells at 6 dpf (Wilcoxon test, $p = 0.49$). Thus, while IL-1β is required to mediate the immediate effects of LPS on branching dynamics and the long-term effects on arbor growth, it is also essential to normal arbor growth and elaboration.

We compared the predatory ability of control MO and IL-1β MO-injected zebrafish. We allowed the larvae to consume paramecia freely for 5 h, recording the number of paramecia remaining each hour. We calculated a prey decline constant for each group (Fig. 8A) and found a significant reduction in the ability of IL-1β MO larvae to consume prey compared with control MO animals. This difference was observed in the presence or absence of LPS treatment at 3 dpf (not shown). IL-1β MO-injected larvae do swim shorter distances than controls (Fig. 8B), although they are capable of comparable acceleration (Fig. 8C). These data suggest that downregulation of IL-1β during development affects not only the visual circuit wiring but likely other systems as well.

Discussion

Our results demonstrate that a single episode of inflammation can have both rapid and long-lasting effects on a developing
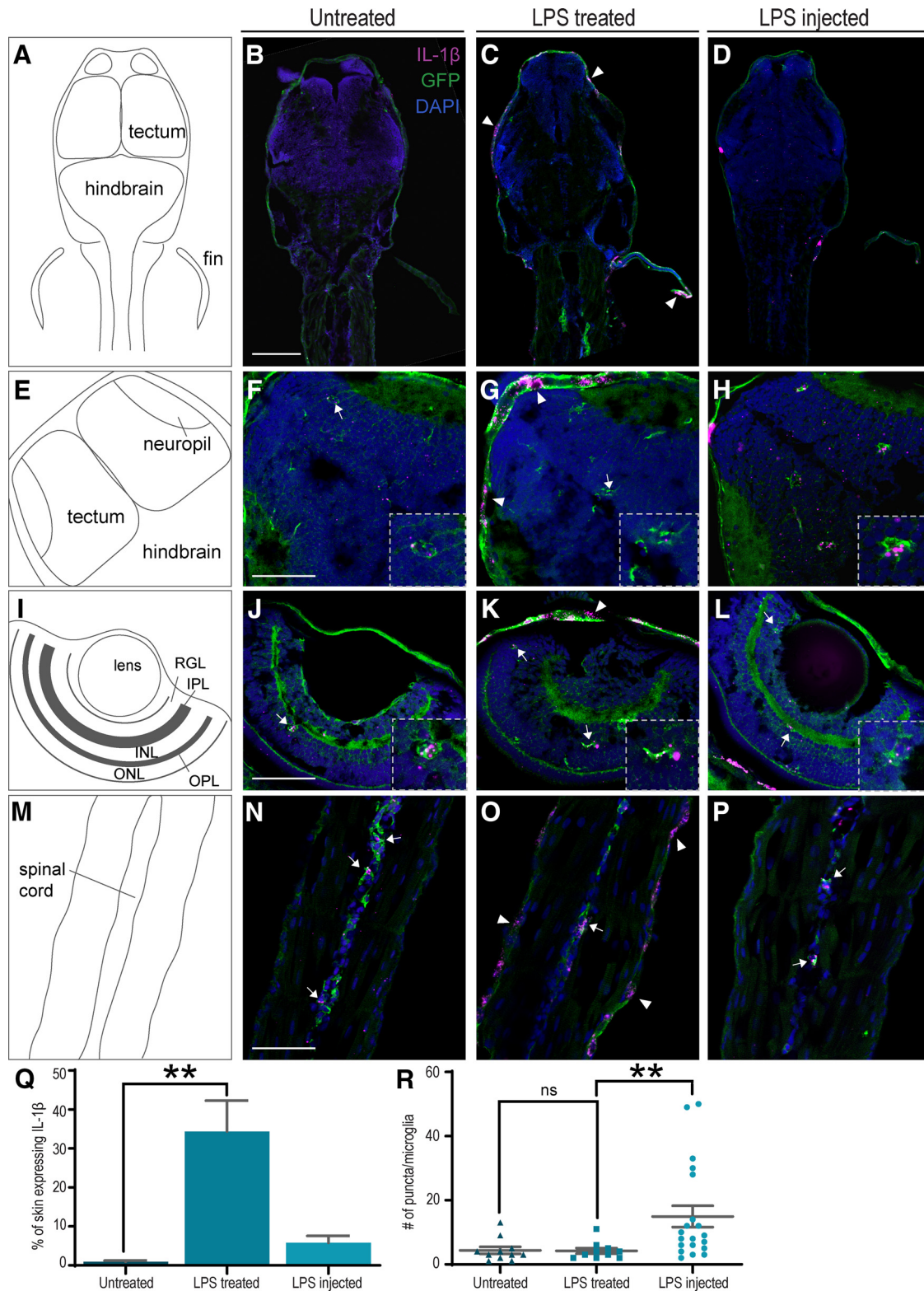
Figure 5. Expression of IL-1β in zebrafish larvae. **A,E,I,M,** Diagrams of the images shown to their right. **B–D,** Anterior half of untreated (**B**), LPS-treated (**C**), or LPS-injected (**D**) 3 dpf larvae. IL-1β expression is observed in the skin of LPS-treated larvae (arrowheads) 2 h after treatment. **F–H,** Expression of IL-1β is observed in microglia (arrows/insets) of untreated (**F**), LPS-treated (**G**), and LPS-injected (**H**) larvae. Expression in patches of skin is also observed in the LPS-treated (arrowhead, **G**) larvae. **J–L,** Microglia in the retina of all 3 larvae also express IL-1β. **N–P,** Microglia in the spinal cord of all 3 larvae express IL-1β. Magenta represents IL-1β (RNAscope). Green represents EGFP (immunohistochemistry). Blue represents DAPI nuclear staining. RGL, RGC layer; IPL, inner plexiform layer; INL, inner nuclear layer; OPL, outer plexiform layer; ONL, outer nuclear layer. **Q,R,** Quantification of the data represented in **A–P**. The percentage of skin that expresses IL-1β mRNA is significantly increased in LPS-treated larvae (**Q**; untreated $n = 4$, LPS-treated $n = 3$, LPS-injected $n = 3$). The number of IL-1β RNAscope puncta is significantly increased in microglia from LPS-injected larvae only (**R**; untreated: $n = 11$, LPS-treated: $n = 10$, LPS-injected: $n = 20$). **$p < 0.01$; Kruskal–Wallis test. Error bars indicate SEM. Scale bars: **B–D**, 100 μm; **F–P**, 50 μm.
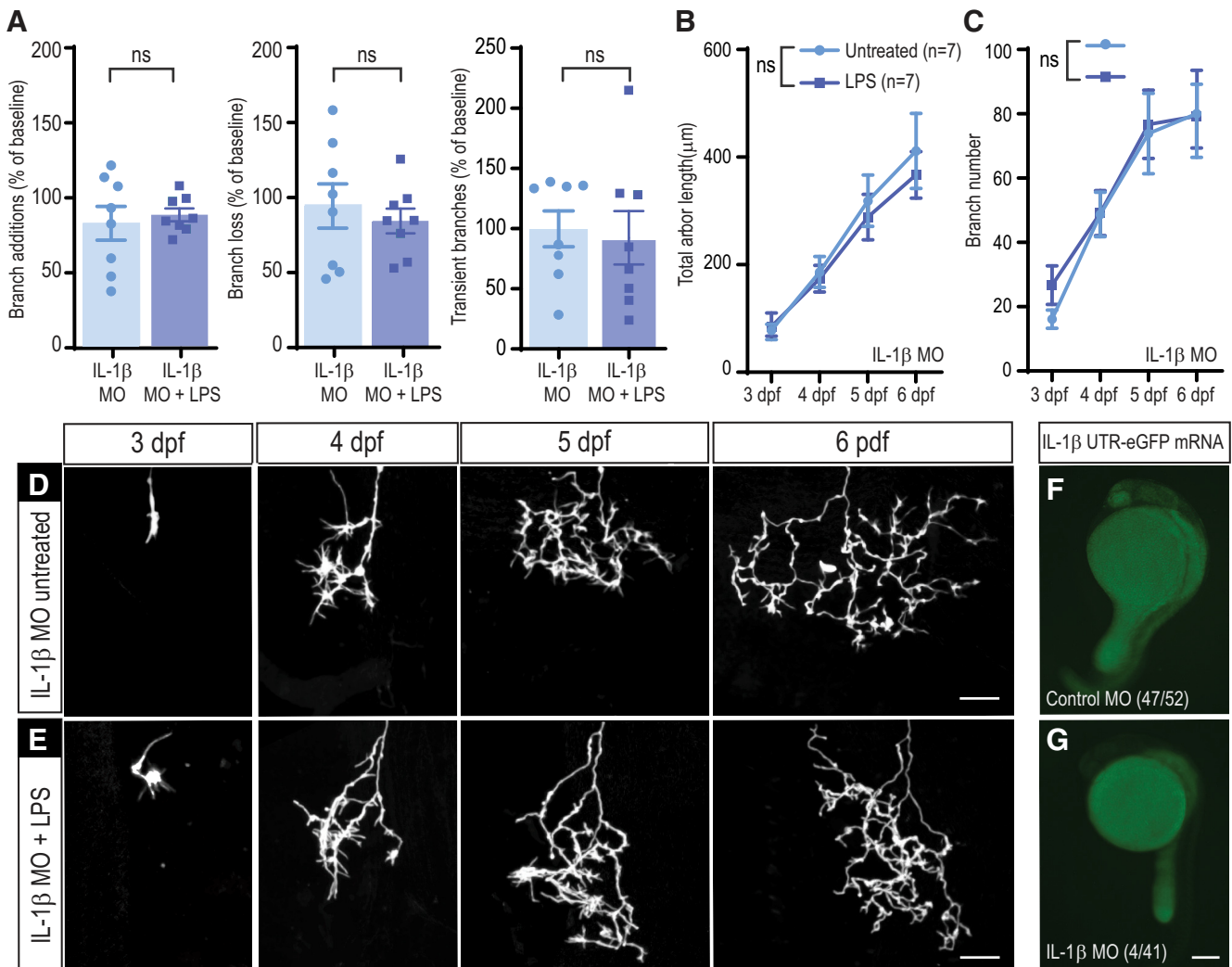
Figure 6. Effects of LPS on RGC arbor growth and elaboration are mediated in part through IL-1β. ***A***, Branching dynamics are not affected by LPS treatment in the absence of IL-1β. The rate of branch additions and branch loss is not significantly different in LPS versus untreated larvae in IL-1β MO-injected animals (*n* = 8 untreated; *n* = 8 LPS); two-way repeated-measures ANOVA. ***B,E***, LPS treatment does not significantly affect the growth of RGC arbors in IL-1β MO-injected larvae. Total arbor length (***B***) and branch number (***C***) are not significantly different from those of untreated control cells (*n* = 7 untreated, *n* = 7 LPS); two-way repeated-measures ANOVA. Single RGCs in embryos injected with IL-1β MO were imaged daily for 4 d following 2 h of mock treatment (IL-1β MO untreated, ***D***) or LPS treatment (IL-1β MO + LPS, ***E***) administered at 3 dpf. ***F,G***, IL-1β MO validation. Embryos were injected with *IL-1β −5'UTR-eGFP* mRNA and control (***F***) or IL-1β MO (***G***). The number of larvae with green fluorescence and the total number of scored larvae are indicated at the bottom of each image. Error bars indicate SEM. Scale bars: ***D,E***, 25 μm; ***F,G***, 200 μm.

nervous system. We detected an increase in axonal dynamics, reflected in the elevated rates of branch addition, branch loss, and in the increased numbers of transient branches, immediately following LPS treatment (Fig. 2). We further observed a significant increase, at 6 dpf, in the size and overall complexity of RGC axons in LPS-treated animals, when mature levels of arborization complexity are normally attained (Fig. 3). These morphologic changes are accompanied by alterations in the responsiveness of the tectal cells to visual stimuli and performance in a simple, tectal-mediated visual behavioral assay (Fig. 4). We also ascertained the contribution of IL-1β, which is markedly but transiently upregulated in response to LPS exposure (Fig. 1F,G), to the effects of inflammatory stimulation on neuronal development. Expression of IL-1β is primarily upregulated in the skin following bath application of LPS but is also expressed in microglia in both untreated and treated larvae (Fig. 5). The immediate and long-term effects on axonal dynamics appear to depend on the production of IL-1β, since they fail to occur when expression of the cytokine is downregulated by MO injection (Fig. 6).

However, the axons in these animals already grow larger and more complex under baseline conditions (Fig. 7), indicating that precise control of IL-1β levels may be critical for regulating RGC axon arbor growth under conditions of inflammatory insult as well as in normal development. These defects contribute to the ineffectiveness of IL-1β morphant larvae in prey capture (Fig. 8).

Dendritic spine analysis through a thinned-skull in the young (postnatal day 17-19) mouse showed decreased dynamics of dendritic spines on layer V pyramidal neurons in the somatosensory cortex following MIA (Coiro et al., 2015). There are important distinctions between our results and those from Coiro et al. (2015), including differences in the brain region of study and the timing of *in vivo* imaging: we observed axonal branching dynamics immediately following the administration of inflammatory stimulus while they imaged dendrites ~1 month after MIA. Moreover, axonal and dendritic dynamics have been reported to exhibit opposite reactions to similar manipulations. For example, pharmacological blockade
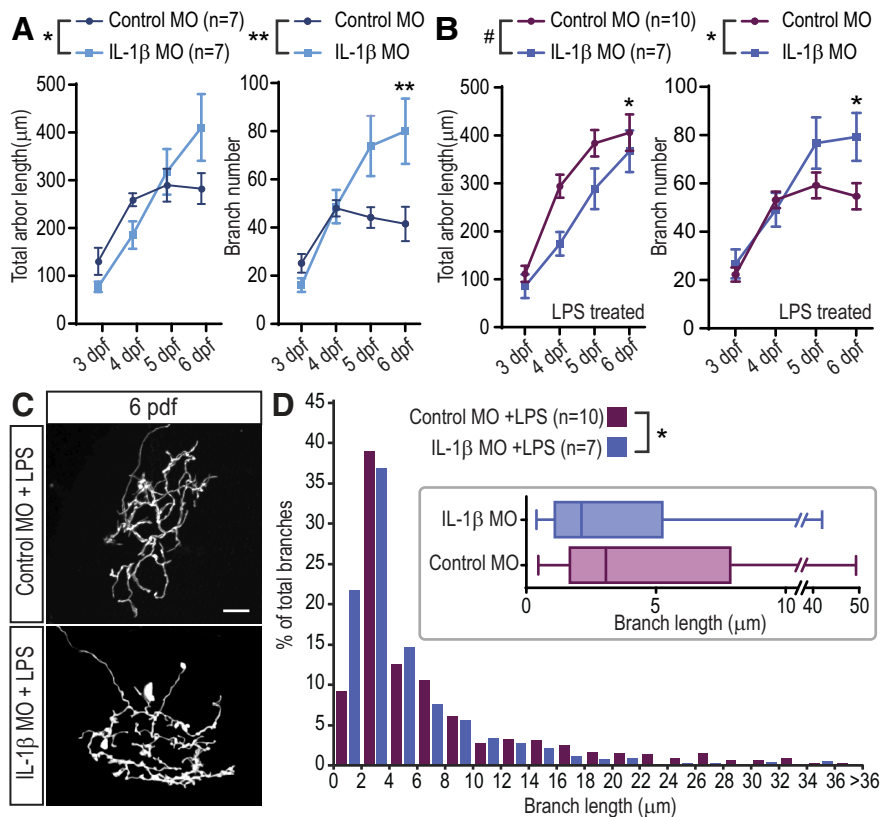
Figure 7. RGC arbors in IL-1β MO-injected animals have abnormal growth. **A**, In the absence of LPS treatment, RGC arbors in IL-1β MO-injected animals display a different growth curve than those from control MO animals. Cells from IL-1β MO-injected animals increase in size slower than control cells but continue to grow until 6 dpf, whereas arbor length of control MO cells plateaus at ∼5 dpf. Cells from IL-1β MO-injected animals add more branches than control MO cells, especially at 5 and 6 dpf. *$p < 0.05$; **$p < 0.01$; two-way repeated-measures ANOVA with Sidak correction for multiple comparisons. **B**, In the presence of LPS, cells from control MO and IL-1β MO-injected animals also have significantly different growth curves, both in total length and in the number of branches added. *$p < 0.05$; **$p < 0.01$; #$p < 0.1$; two-way repeated-measures ANOVA with Sidak correction for multiple comparisons. **C,D**, RGC arbors in IL-1β MO-injected animals have a greater number of very small branches at 6 dpf. The size distribution of all RGC branches from control MO and IL-1β MO-injected animals is significantly different, as measured at 6 dpf in LPS-treated animals, and illustrated in the inset in **D**). *$p < 0.05$; Wilcoxon test. Error bars indicate SEM. Scale bars, 25 μm.
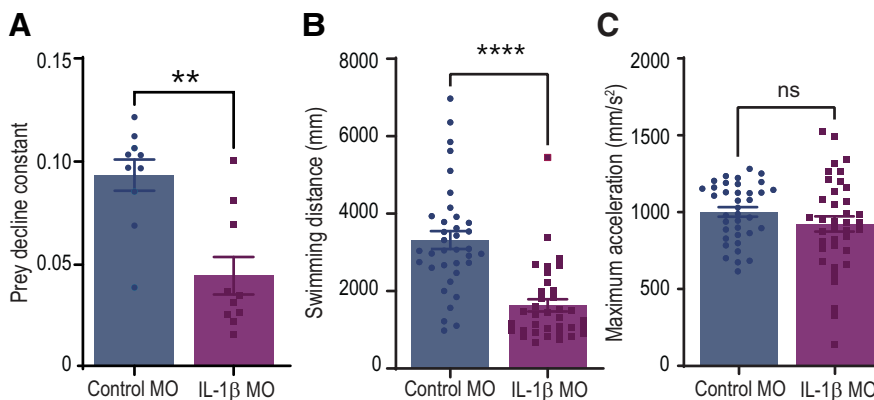

Figure 8. IL-1β morphant zebrafish larvae are poor predators. **A**, IL-1β MO-injected zebrafish larvae consume paramecia more slowly than their control MO-injected siblings. **B**, IL-1β MO-injected animals swim a smaller distance per unit time than those injected with control MO. **C**, Maximum acceleration during larval swimming is unaffected by MO injection. **$p < 0.01$; ****$p < 0.0001$; Kruskal–Wallis test. Error bars indicate SEM.

Studies in rodent models of MIA have shown disparate effects of inflammation on neuronal growth. In rats from litters treated with LPS to induce inflammation during gestation, dendritic arbor size was reduced in layer V mPFC neurons from young (P10, P35) animals, but returned to values no different from control at P60, while CA1 hippocampal neurons showed reduced dendritic length only in adult animals (Baharnoori et al., 2009). Spine density was found to be significantly lower in pyramidal neurons in mPFC in P60 MIA animals (Baharnoori et al., 2009). In another study also using LPS-induced MIA in rats, spine density of dentate gyrus granule cells was increased at P21 but decreased at P90 (Lin and Wang, 2014). Granule cells in the hippocampus showed a significant increase in spine density and a nonsignificant increase in the number of branching nodes in P15 males from litters treated with LPS at embryonic day 15 (E15) (Fernández de Cossío et al., 2017). Hence, inflammatory stimulation during development affects neuronal populations in complex ways.

Studies in postmortem brain samples from ASD patients have detected differences in neuronal morphology compared with controls. Of note, a reduction in the number of dendrites in hippocampal and PFC neurons was observed compared with normally developing controls (Raymond et al., 1996; Mukaetova-Ladinska et al., 2004). Conversely, a higher density of axons has been described in the serotonin pathways of ASD subjects (Azmitia et al., 2011). Spine density alterations in ASD patients also vary. A decrease in spine density found on pyramidal neurons in the neocortex (Williams et al., 1980) is in contrast with an increase in spine density on apical dendrites of layer II pyramidal neurons in the frontal, temporal, and parietal cortex as well as layer V neurons of the temporal cortex (Hutsler and Zhang, 2010). Spine density and total dendritic length of pyramidal neurons in the dorsolateral PFC of schizophrenia subjects were also reduced compared with normal brain samples (Glantz and Lewis, 2000). Given that various neuron populations are affected differently at different developmental time points, it would be useful to better understand how visual system pathways may be affected in rodent models and in human patients. For example, direct administration of pro-inflammatory cytokine, such as intravitreous injection of IL-6 in rats, has been shown to result in abnormal spreading of RGC axons in the superior colliculus (Menezes et al., 2019).

or postsynaptic morpholino knockdown of NMDA-type glutamate receptors in the retinotectal system of *Xenopus* tadpoles impedes dendritic growth while enhancing axonal dynamics (Rajan et al., 1999; Sin et al., 2002; Kesner et al., 2020).

We have shown that the morphologic changes we observed in the RGC axons following inflammatory stimulation are accompanied by functional alterations in the retinotectal circuit and performance in a simple behavioral assay (Fig. 4). One of the hallmarks of ASD is a demonstrated hypersensitivity to sensory stimulation, including visual stimuli (Takarae and Sweeney, 2017). Studies in ASD patients have assessed aspects of low-level visual processing (Bakroon and Lakshminarayanan, 2016; Robertson and Baron-Cohen, 2017), although high variability in the methods used and small sample sizes make it difficult to compare results across reports. Nevertheless, some studies have found that ASD patients show enhanced perception of high spatial frequency visual cues (Kéïta et al., 2014; Caplette et al., 2016), in line with a large body of evidence for enhanced overall visual functioning in autism (Samson et al., 2012). In contrast, it is suspected that schizophrenia patients may have lower visual acuity (Silverstein and Rosen, 2015), and impairments in contrast perception and processing (Butler et al., 2001). Therefore, our data showing an altered response to luminance levels and decreased visual acuity in LPS-treated zebrafish larvae may be relevant to the etiology of ASD and schizophrenia. We have developed a simple developmental inflammation model in a fast-growing, genetically amenable animal, which at least partially recapitulates aspects of neurodevelopmental disorders, with the hope that it may serve as a platform to explore the molecular underpinnings of such functional pathologies.

Our results demonstrate an important role for IL-1β in mediating the acute and long-term effects of inflammatory insult on RGC development (Fig. 6). The evidence that a predominant source of excess IL-1β in our LPS-treated larvae is the skin (Fig. 5) is of particular relevance to MIA. In a study using polyinosinic:polycytidylic acid-induced inflammation in the mouse, levels of certain cytokines, including IL-6 and TNF-α, were increased in maternal plasma, placenta, and fetal brain, while IL-1β was upregulated in maternal plasma only (Mueller et al., 2019). Here we show that external application of an inflammatory stimulus and a peripheral activation of IL-1β are sufficient to cause short- and long-term changes to neuronal circuit development, suggesting that additional downstream signaling molecules likely mediate the central changes.

We also demonstrate a role for IL-1β signaling in the normal growth of RGCs, since these axons develop abnormally in IL-1β knockdown larvae, even in the absence of LPS treatment (Fig. 7). Indeed, RCG axons from IL-1β MO animals have more branches at 6 dpf than control MO cells (Fig. 7A,B). Moreover, the branch size distribution is significantly different between IL-1β MO and control MO axons (Fig. 7D). Cytokines have demonstrated roles beyond inflammatory responses, including in synaptic plasticity, neurogenesis, and neuromodulation (McAfoose and Baune, 2009). TNF-α exposure promotes synaptic maturation, resulting in an increase in spontaneous synaptic event frequency, and enhanced dendritic branch growth in neurons in the optic tectum of *Xenopus laevis* tadpoles (Lee et al., 2010). Recombinant IL-1β has been shown to promote differentiation and neurite outgrowth of neuronal precursor cells *in vitro* (Park et al., 2018) and in entorhinal brain slice cultures from P2 mice (Boato et al., 2011), consistent with a role in normal development. In contrast, male rats chronically overexpressing IL-1β through lentiviral injection had reduced neurite length of doublecortin-expressing immature neurons (Hueston et al., 2018).

Although microglia do not appear to be the primary source of IL-1β upregulation in our inflammation model (Fig. 5), we have

shown that their morphology is modified immediately following LPS treatment, demonstrating that they respond to the insult (Fig. 1B–E). Microglia in close proximity to the skin or vasculature may be the first to sense the elevated IL-1β levels and in turn upregulate other cytokines. Microglia have been shown to perform numerous tasks in neurodevelopment, both in normal conditions and in mediating the effects of inflammation, through direct physical contact and secretion of signaling molecules (Tay et al., 2017; Lenz and Nelson, 2018; Konishi et al., 2019; Lim and Ruthazer, 2021). Detailed characterization of the role of microglia in mediating the effects of inflammation on neuronal development in our model will contribute significantly to the field of MIA and continue to advance our understanding of the etiology of neurodevelopmental disorders, such as ASD and schizophrenia.

References

Anketell PM, Saunders KJ, Gallagher SM, Bailey C, Little JA (2015) Brief report: vision in children with autism spectrum disorder: what should clinicians expect? J Autism Dev Disord 45:3041–3047.

Atladóttir HÓ, Thorsen P, Østergaard L, Schendel DE, Lemcke S, Abdallah M, Parner ET (2010) Maternal infection requiring hospitalization during pregnancy and autism spectrum disorders. J Autism Dev Disord 40:1423–1430.

Azmitia EC, Singh JS, Whitaker-Azmitia PM (2011) Increased serotonin axons (immunoreactive to 5-HT transporter) in postmortem brains from young autism donors. Neuropharmacology 60:1347–1354.

Baharnoori M, Brake WG, Srivastava LK (2009) Prenatal immune challenge induces developmental changes in the morphology of pyramidal neurons of the prefrontal cortex and hippocampus in rats. Schizophr Res 107:99–109.

Bakroon A, Lakshminarayanan V (2016) Visual function in autism spectrum disorders: a critical review. Clin Exp Optom 99:297–308.

Banerjee S, Leptin M (2014) Systemic response to ultraviolet radiation involves induction of leukocytic IL-1 and inflammation in zebrafish. J Immunol 193:1408–1415.

Boato F, Hechler D, Rosenberger K, Lüdecke D, Peters EM, Nitsch R, Hendrix S (2011) Interleukin-1 beta and neurotrophin-3 synergistically promote neurite growth in vitro. J Neuroinflammation 8:183.

Boato F, Rosenberger K, Nelissen S, Geboes L, Peters EM, Nitsch R, Hendrix S (2013) Absence of IL-1β positively affects neurological outcome, lesion development and axonal plasticity after spinal cord injury. J Neuroinflammation 10:6.

Brown AS, Derkits EJ (2010) Prenatal infection and schizophrenia: a review of epidemiologic and translational studies. Am J Psychiatry 167:261–280.

Butler PD, Schechter I, Zemon V, Schwartz SG, Greenstein VC, Gordon J, Schroeder CE, Javitt DC (2001) Dysfunction of early-stage visual processing in schizophrenia. Am J Psychiatry 158:1126–1133.

Caplette L, Wicker B, Gosselin F (2016) Atypical time course of object recognition in autism spectrum disorder. Sci Rep 6:35494.

Chen CM, Yang P, Wu MT, Chuang TC, Huang TY (2019) Deriving and validating biomarkers associated with autism spectrum disorders from a large-scale resting-state database. Sci Rep 9:10.

Christou-Savina S, Beales PL, Osborn DP (2015) Evaluation of zebrafish kidney function using a fluorescent clearance assay. J Vis Exp 96:e52540.

Coiro P, Padmashri R, Suresh A, Spartz E, Pendyala G, Chou S, Jung Y, Meays B, Roy S, Gautam N, Alnouti Y, Li M, Dunaevsky A (2015) Impaired synaptic development in a maternal immune activation mouse model of neurodevelopmental disorders. Brain Behav Immun 50:249–258.

Coupé P, Munz M, Manjón JV, Ruthazer ES, Collins DL (2012) A CANDLE for a deeper in vivo insight. Med Image Anal 16:849–864.

Estes ML, McAllister AK (2016) Maternal immune activation: implications for neuropsychiatric disorders. Science 353:772–777.

Fernández de Cossío L, Guzmán A, van der Veldt S, Luheshi GN (2017) Prenatal infection leads to ASD-like behavior and altered synaptic pruning in the mouse offspring. Brain Behav Immun 63:88–98.

Glantz LA, Lewis DA (2000) Decreased dendritic spine density on prefrontal cortical pyramidal neurons in schizophrenia. Arch Gen Psychiatry 57:65–73.

Hasegawa T, Hall CJ, Crosier PS, Abe G, Kawakami K, Kudo A, Kawakami A (2017) Transient inflammatory response mediated by interleukin-1β is required for proper regeneration in zebrafish fin fold. Elife 6:e22716.

Heinsfeld AS, Franco AR, Craddock RC, Buchweitz A, Meneguzzi F (2018) Identification of autism spectrum disorder using deep learning and the ABIDE dataset. Neuroimage Clin 17:16–23.

Hueston CM, O'Leary JD, Hoban AE, Kozareva DA, Pawley LC, O'Leary OF, Cryan JF, Nolan YM (2018) Chronic interleukin-1β in the dorsal hippocampus impairs behavioural pattern separation. Brain Behav Immun 74:252–264.

Hutsler JJ, Zhang H (2010) Increased dendritic spine densities on cortical projection neurons in autism spectrum disorders. Brain Res 1309:83–94.

Ikegaya Y, Delcroix I, Iwakura Y, Matsuki N, Nishiyama N (2003) Interleukin-1β abrogates long-term depression of hippocampal CA1 synaptic transmission. Synapse 47:54–57.

Jack A (2018) Neuroimaging in neurodevelopmental disorders: focus on resting-state fMRI analysis of intrinsic functional brain connectivity. Curr Opin Neurol 31:140–148.

Kéïta L, Guy J, Berthiaume C, Mottron L, Bertone A (2014) An early origin for detailed perception in autism spectrum disorder: biased sensitivity for high-spatial frequency information. Sci Rep 4:5475–5419.

Kesner P, Schohl A, Warren EC, Ma F, Ruthazer ES (2020) Postsynaptic and presynaptic NMDARs have distinct roles in visual circuit development. Cell Rep 32:107955.

Khandaker GM, Cousins L, Deakin J, Lennox BR, Yolken R, Jones PB (2015) Inflammation and immunity in schizophrenia: implications for pathophysiology and treatment. Lancet Psychiatry 2:258–270.

Khosravani N, Goodarzi MA (2013) Patients with schizophrenia show deficits on spatial frequency doubling. Vision Res 93:49–53.

King DJ, Hodgekins J, Chouinard PA, Chouinard VA, Sperandio I (2017) A review of abnormalities in the perception of visual illusions in schizophrenia. Psychon Bull Rev 24:734–751.

Konishi H, Kiyama H, Ueno M (2019) Dual functions of microglia in the formation and refinement of neural circuits during development. Int J Dev Neurosci 77:18–25.

Lee RH, Mills EA, Schwartz N, Bell MR, Deeg KE, Ruthazer ES, Marsh-Armstrong N, Aizenman CD (2010) Neurodevelopmental effects of chronic exposure to elevated levels of pro-inflammatory cytokines in a developing visual system. Neural Dev 5:2.

Lenz KM, Nelson LH (2018) Microglia and beyond: innate immune cells as regulators of brain development and behavioral function. Front Immunol 9:698.

Lim TK, Ruthazer ES (2021) Microglial trogocytosis and the complement system regulate axonal pruning in vivo. eLife 10:e62167.

Lin YL, Wang S (2014) Prenatal lipopolysaccharide exposure increases depression-like behaviors and reduces hippocampal neurogenesis in adult rats. Behav Brain Res 259:24–34.

Livak KJ, Schmittgen TD (2001) Analysis of relative gene expression data using real-time quantitative PCR and the 2−ΔΔCT method. Methods 25:402–408.

Marín O, Rubenstein JL (2001) A long, remarkable journey: tangential migration in the telencephalon. Nat Rev Neurosci 2:780–790.

McAfoose J, Baune BT (2009) Evidence for a cytokine model of cognitive function. Neurosci Biobehav Rev 33:355–366.

Menezes GD, Faria-Melibeu AC, Serfaty CA, Campello-Costa P (2019) In vivo effect of acute exposure to interleukin-6 on the developing visual system. Neurosci Lett 698:7–12.

Meyer U, Feldon J, Dammann O (2011) Schizophrenia and autism: both shared and disorder-specific pathogenesis via perinatal inflammation? Pediatr Res 69:26–33.

Morrison HW, Filosa JA (2013) A quantitative spatiotemporal analysis of microglia morphology during ischemic stroke and reperfusion. J Neuroinflammation 10:4.

Mottahedin A, Ardalan M, Chumak T, Riebe I, Ek J, Mallard C (2017) Effect of neuroinflammation on synaptic organization and function in the developing brain: implications for neurodevelopmental and neurodegenerative disorders. Front Cell Neurosci 11:190.

Mueller FS, Richetto J, Hayes LN, Zambon A, Pollak DD, Sawa A, Meyer U, Weber-Stadlbauer U (2019) Influence of poly(I:C) variability on

thermoregulation, immune responses and pregnancy outcomes in mouse models of maternal immune activation. Brain Behav Immun 80:406–418.

Mukaetova-Ladinska EB, Arnold H, Jaros E, Perry R, Perry E (2004) Depletion of MAP2 expression and laminar cytoarchitectonic changes in dorsolateral prefrontal cortex in adult autistic individuals. Neuropathol Appl Neurobiol 30:615–623.

Müller N, Weidinger E, Leitner B, Schwarz MJ (2015) The role of inflammation in schizophrenia. Front Neurosci 9:372.

Nakagawa Y, Chiba K (2016) Involvement of neuroinflammation during brain development in social cognitive deficits in autism spectrum disorder and schizophrenia. J Pharmacol Exp Ther 358:504–515.

Novoa B, Bowman TV, Zon L, Figueras A (2009) LPS response and tolerance in the zebrafish (*Danio rerio*). Fish Shellfish Immunol 26:326–331.

Orger MB, Gahtan E, Muto A, Page-McCaw P, Smear MC, Baier H (2004) Behavioral screening assays in zebrafish. Methods Cell Biol 77:53–68.

Park S, Kang M, Han J (2018) Interleukin-1 beta promotes neuronal differentiation through the Wnt5a/RhoA/JNK pathway in cortical neural precursor cells. Mol Brain 11:12.

Patterson BW, Abraham AO, MacIver MA, McLean DL (2013) Visually guided gradation of prey capture movements in larval zebrafish. J Exp Biol 216:3071–3083.

Peri F, Nüsslein-Volhard C (2008) Live imaging of neuronal degradation by microglia reveals a role for v0-ATPase a1 in phagosomal fusion in vivo. Cell 133:916–927.

Poulain FE, Gaynes JA, Hörndli CS, Law MY, Chien CB (2010) Analyzing retinal axon guidance in zebrafish. Methods Cell Biol 100:3–26.

Rajan I, Witte S, Cline HT (1999) NMDA receptor activity stabilizes presynaptic retinotectal axons and postsynaptic optic tectal cell dendrites in vivo. J Neurobiol 38:357–368.

Raymond GV, Bauman ML, Kemper TL (1996) Hippocampus in autism: a Golgi analysis. Acta Neuropathol 91:117–119.

Robbins JR, Bakardjiev AI (2012) Pathogens and the placental fortress. Curr Opin Microbiol 15:36–43.

Robertson CE, Baron-Cohen S (2017) Sensory perception in autism. Nat Rev Neurosci 18:671–684.

Robertson CE, Thomas C, Kravitz DJ, Wallace GL, Baron-Cohen S, Martin A, Baker CI (2014) Global motion perception deficits in autism are reflected as early as primary visual cortex. Brain 137:2588–2599.

Samson F, Mottron L, Soulières I, Zeffiro TA (2012) Enhanced visual functioning in autism: an ALE meta-analysis. Hum Brain Mapp 33:1553–1581.

Schneider H, Pitossi F, Balschun D, Wagner A, Del Rey A, Besedovsky HO (1998) A Neuromodulatory role of interleukin-1β in the hippocampus. Proc Natl Acad Sci USA 95:7778–7783.

Schroeter EH, Wong RO, Gregg RG (2006) In vivo development of retinal ON-bipolar cell axonal terminals visualized in nyx::MYFP transgenic zebrafish. Vis Neurosci 23:833–843.

Silverstein SM, Rosen R (2015) Schizophrenia and the eye. Schizophr Res Cogn 2:46–55.

Simmons DR, Robertson AE, McKay LS, Toal E, McAleer P, Pollick FE (2009) Vision in autism spectrum disorders. Vision Res 49:2705–2739.

Sin WC, Haas K, Ruthazer ES, Cline HT (2002) Dendrite growth increased by visual activity requires NMDA receptor and Rho GTPases. Nature 419:475–480.

Smear MC, Tao HW, Staub W, Orger MB, Gosse NJ, Liu Y, Takahashi K, Poo MM, Baier H (2007) Vesicular glutamate transport at a central synapse limits the acuity of visual perception in zebrafish. Neuron 53:65–77.

Solek CM, Farooqi N, Verly M, Lim TK, Ruthazer ES (2018) Maternal immune activation in neurodevelopmental disorders. Dev Dyn 247:588–619.

Stuart MJ, Singhal G, Baune BT (2015) Systematic review of the neurobiological relevance of chemokines to psychiatric disorders. Front Cell Neurosci 9:357.

Svahn AJ, Graeber MB, Ellett F, Lieschke GJ, Rinkwitz S, Bennett MR, Becker TS (2013) Development of ramified microglia from early macrophages in the zebrafish optic tectum. Dev Neurobiol 73:60–71.

Takarae Y, Sweeney J (2017) Neural hyperexcitability in autism spectrum disorders. Brain Sci 7:129.

Tay TL, Savage JC, Hui CW, Bisht K, Tremblay MÈ (2017) Microglia across the lifespan: from origin to function in brain development, plasticity and cognition. J Physiol 595:1929–1917.

Varghese M, Keshav N, Jacot-Descombes S, Warda T, Wicinski B, Dickstein DL, Harony-Nicolas H, de Rubeis S, Drapeau E, Buxbaum JD, Hof PR

(2017) Autism spectrum disorder: neuropathology and animal models. Acta Neuropathol 134:537–566.

Vezzani A, Viviani B (2015) Neuromodulatory properties of inflammatory cytokines and their impact on neuronal excitability. Neuropharmacology 96:70–82.

Vladimirov N, Mu Y, Kawashima T, Bennett DV, Yang CT, Looger LL, Keller PJ, Freeman J, Ahrens MB (2014) Light-sheet functional imaging in fictively behaving zebrafish. Nat Methods 11:883–882.

Westerfield M (2000) The zebrafish book: a guide for the laboratory use of zebrafish (Danio rerio), Ed 4. Eugene, OR: University of Oregon.

Williams RS, Hauser SL, Purpura DP, DeLong GR, Swisher CN (1980) Autism and mental retardation: neuropathologic studies performed in four retarded persons with autistic behavior. Arch Neurol 37: 749–753.

Xiao T, Roeser T, Staub W, Baier H (2005) A GFP-based genetic screen reveals mutations that disrupt the architecture of the zebrafish retinotectal projection. Development 132:2955–2967.

Xie Y, Meijer AH, Schaaf MJ (2021) Modeling inflammation in zebrafish for the development of anti-inflammatory drugs. Front Cell Dev Biol 8:620984.

Yang LL, Wang GQ, Yang LM, Huang ZB, Zhang WQ, Yu LZ (2014) Endotoxin molecule lipopolysaccharide-induced zebrafish inflammation model: a novel screening method for anti-inflammatory drugs. Molecules 19:2390–2409.